



Published in final edited form as:

Nat Commun. ; 5: 4667. doi:10.1038/ncomms5667.

Molecular Determinants of Magnesium-Dependent Synaptic Plasticity at Electrical Synapses Formed by Connexin36

Nicolás Palacios-Prado^{1,2,*}, Sandrine Chapuis¹, Alejandro Panjkovich³, Julien Fregeac¹, James I. Nagy⁴, and Feliksas F. Bukauskas^{1,*}

¹Dominick P. Purpura Department of Neuroscience, Albert Einstein College of Medicine, NY 10461, USA

²Grass Laboratory, Marine Biological Laboratory, Woods Hole, MA 02543, USA

³European Molecular Biology Laboratory, Hamburg Outstation, 22603 Hamburg, Germany

⁴Department of Physiology, University of Manitoba, Winnipeg, Manitoba R3E 0J9, Canada

Abstract

Neuronal gap junction (GJ) channels composed of connexin36 (Cx36) play an important role in neuronal synchronization and network dynamics. Here we show that Cx36-containing electrical synapses between inhibitory neurons of the thalamic reticular nucleus are bi-directionally modulated by changes in intracellular free magnesium concentration ($[Mg^{2+}]_i$). Chimeragenesis demonstrates that the first extracellular loop of Cx36 contains a Mg^{2+} -sensitive domain, and site-directed mutagenesis shows that the pore-lining residue D47 is critical in determining high Mg^{2+} -sensitivity. Single channel analysis of Mg^{2+} -sensitive chimeras and mutants reveals that $[Mg^{2+}]_i$ controls the strength of electrical coupling mostly via gating mechanisms. In addition, asymmetric transjunctional $[Mg^{2+}]_i$ induces strong instantaneous rectification, providing a novel mechanism for electrical rectification in homotypic Cx36 GJs. We suggest that Mg^{2+} -dependent synaptic plasticity of Cx36-containing electrical synapses could underlie neuronal circuit reconfiguration via changes in brain energy metabolism that affects neuronal levels of intracellular ATP and $[Mg^{2+}]_i$.

Introduction

Magnesium is the second most abundant intracellular cation after potassium, and is a critical cofactor in many enzymatic reactions involving energy metabolism. Magnesium is highly

Users may view, print, copy, and download text and data-mine the content in such documents, for the purposes of academic research, subject always to the full Conditions of use:http://www.nature.com/authors/editorial_policies/license.html#terms

*Correspondence and requests for materials should be addressed to N.P.-P. (nicolas.palacios-prado@phd.einstein.yu.edu) or F.F.B. (feliksas.bukauskas@einstein.yu.edu).

Author contribution: N.P.-P. and F.F.B. conceived and designed the experiments. N.P.-P., S.C., J.F. and F.F.B. performed the experiments and analyzed the data. A.P. and J.I.N. contributed reagents/materials/analysis tools and critically revised the paper. N.P.-P. and F.F.B. coordinated the study and wrote the paper.

Additional Information

Supplementary Information accompanies this paper at...

Competing financial interests: The authors declare no competing financial interests.

concentrated in cellular organelles, such as mitochondria, nucleus and endoplasmic reticulum, and it binds to several ionic cytoplasmic constituents. Importantly, phosphonucleotides, such as ATP, bind magnesium ions (MgATP^{2-}) and the enzymatic hydrolysis of their phosphate groups depends on this interaction¹. Therefore, the intracellular concentration of free magnesium ($[\text{Mg}^{2+}]_i$) is closely related to cell bioenergetics and is expected to vary according to the state of cellular metabolism and levels of intracellular ATP². Resting $[\text{Mg}^{2+}]_i$ is less than 10% of total cellular magnesium, and it ranges from 0.2 to 3.5 mM in neurons depending on cell type and species^{3,4,5}. Under physiological conditions, depolarization triggers an increase of $[\text{Mg}^{2+}]_i$ in sensory neurons⁶, while glutamate exposure induces a $[\text{Mg}^{2+}]_i$ surge in forebrain and hippocampal neurons^{7,8}. More recently, it was shown that activation of a nitric oxide signaling pathway can also trigger an increase of $[\text{Mg}^{2+}]_i$ in hippocampal neurons⁹. Moreover, enhanced $[\text{Mg}^{2+}]_i$ can be expected with a reduction in the levels of ATP during periods of waking and hyperactivity¹⁰. Conversely, reduction in $[\text{Mg}^{2+}]_i$ can be expected with an increase in ATP levels during glucose or lactate exposure¹¹ and during the first hours of sleep¹⁰. In pathological conditions, early onset of ischemic cell death is mainly due to the inability of mitochondria to produce ATP, resulting in the failure to regulate transmembrane ion gradients¹², which impacts $[\text{Mg}^{2+}]_i$. Long-lasting elevation in brain $[\text{Mg}^{2+}]_i$ occurs in some acute and chronic brain pathologies such as hypoxia/ischemia^{13,14} and in patients with schizophrenia¹⁵. In contrast, $[\text{Mg}^{2+}]_i$ is reduced after traumatic brain injury^{16,17} and in patients with Parkinson¹⁸, Alzheimer¹⁹, multiple sclerosis²⁰, amyotrophic lateral sclerosis²¹, chronic migraine²² and mitochondrial diseases²³.

Electrical synapses are specialized intercellular junctions formed by clusters of gap junction (GJ) channels that allow bidirectional electrotonic signaling between neurons. Many roles for electrical synapses have been documented, such as synchronization and coordination of neuronal networks²⁴, memory formation²⁵ and lateral excitation in olfactory glomeruli²⁶. GJ channels are formed by the connexin (Cx) and innexin gene families in vertebrates and invertebrates, respectively. Six Cx (or innexin) proteins oligomerize into a pore-forming hemichannel (HC), and the docking of two HCs contributed by adjacent cells forms a GJ channel. The docking of HCs from apposing cells containing the same Cx type results in homotypic GJs, while the docking of HCs containing different Cxs results in heterotypic GJs. Sensitivity of junctional conductance (g_j) to transjunctional voltage (V_j) is a common property of all GJs. Each apposed/junctional HC (aHC) has two distinct V_j -sensitive gates that are responsible for the steady-state g_j - V_j relationship ($g_{j,ss}$ - V_j). This relationship is typically symmetric for either polarity of V_j in homotypic junctions²⁷, but asymmetric in heterotypic junctions where aHCs have V_j -sensitivity and/or single channel conductance differences, which leads to an asymmetry in electrical signal transfer and metabolic communication^{28,29}. An instantaneous g_j - V_j relationship ($g_{j,inst}$ - V_j), however, is more relevant with respect to electrical synapses since neuronal membrane potential fluctuates in the ms time scale during action potentials. Many electrical synapses rectify instantaneously^{30,31,32,33}; i.e. electrical signals are preferentially transmitted anterogradely or retrogradely. Electrical synapses between neurons in the mammalian CNS are typically formed by Cx36³⁴, which is commonly expressed throughout the CNS^{34,35}. Modulation of electrical synapses can occur by different factors such as phosphorylation^{36,37}, changes in

pH³⁸ and exposure to lipophilic molecules³⁹. Interestingly, Cx36-containing electrical synapses can undergo activity-dependent long-term depression⁴⁰, or CaMKII- and PKA-dependent long-term potentiation^{41,42}.

We recently reported a novel Mg²⁺-dependent form of electrical synaptic plasticity between neurons of the trigeminal mesencephalic nucleus (MesV) and in heterologous expression systems transfected with Cx36⁴³. We showed that the strength of electrical synaptic transmission is augmented or reduced by low or high [Mg²⁺]_i, respectively. The g_j of GJs formed of Cxs 26, 30.2, 32, 36, 43, 45, 47, and 57 expressed in HeLa cells was reduced by increasing [Mg²⁺]_i, whereas lowering [Mg²⁺]_i increased g_j only in Cx36 expressing cells, indicating that Cx36 GJs are strongly inhibited by normal/resting [Mg²⁺]_i. We also demonstrated that Mg²⁺ ions are permeable to Cx36 GJs and an effect of Mg²⁺ on g_j is fully reversible⁴³.

Here, we show that electrical synapses formed by Cx36 in the thalamic reticular nucleus (TRN) are also bi-directionally modulated by changes in [Mg²⁺]_i and that an altered Mg-ATP equilibrium can trigger Mg²⁺-dependent plasticity of neuronal electrical coupling. We sought to locate the molecular domains of Cx36 GJ channels that contribute to such unusually high sensitivity to [Mg²⁺]_i using chimeragenesis and site-directed mutagenesis. Our data show that a negatively-charged aspartate (D47), located in the first extracellular loop (E1), is responsible for high Mg²⁺-sensitivity. Single channel analysis of chimeras reveals that changes in [Mg²⁺]_i affect the voltage-dependent gating of channels without changing the single channel conductance. We also found that [Mg²⁺]_i modulates the $g_{j,inst}-V_j$ dependence of Cx36 GJs by producing a hyperbolic $g_{j,inst}-V_j$ relationship that is unique to Cx36 GJs. Previously, we showed that asymmetry in the transjunctional [Mg²⁺]_i results in an asymmetry of steady-state g_j ($g_{j,ss}$) dependence on V_j .⁴³ We now demonstrate that asymmetry in the transjunctional [Mg²⁺]_i results in an asymmetric $g_{j,inst}-V_j$ relationship of homotypic Cx36 GJ channels. Hence, the intercellular gradient of divalent cations, such as Mg²⁺, is a novel mechanism that can generate instantaneous rectification in homotypic Cx36 GJs. In addition, we show that the second extracellular loop (E2) is an important molecular component that contributes to the incompatibility between neuronal Cx36 and astrocytic Cx43 HCs to dock and form functional heterotypic GJs.

Results

Electrical synapses in the TRN are modulated by [Mg²⁺]_i

To test whether native electrical synapses expressing Cx36 are sensitive to changes in [Mg²⁺]_i, we used a BAC transgenic mouse line (Tg(*Gjd2-EGFP*)JM16Gsat/Mmucd)⁴⁴, in which expression of the EGFP reporter gene is driven by the promoter of Cx36 and expression of the endogenous Cx36 protein is left intact. In *Gjd2-EGFP* mice, one can easily identify EGFP-positive neurons, facilitating the selection of adjacent pairs of electrically-coupled neurons for electrophysiological analysis. The TRN was chosen for examination due to its relatively high incidence of electrical coupling⁴⁵. It is a diencephalic layer of GABAergic interneurons that forms a capsule around the ventrobasal (VB) complex of the thalamus, and plays an important role in switching states of arousal and consciousness⁴⁶. Acute horizontal slices of mouse thalamus were used for confocal fluorescence imaging of

the TRN (Fig. 1a,b) and for measuring g_j using a dual whole-cell patch clamp (Fig. 1c) in pairs of neurons displaying EGFP fluorescence (Fig. 1d). From a total of 57 neuronal pairs recorded, 18 pairs were electrically coupled (31.6%). The intrinsic firing properties (Fig. 1e) and attenuated evoked responses (Supplementary Fig. 1) of electrically coupled EGFP-expressing neurons were similar to those previously reported⁴⁵. To reduce or increase $[Mg^{2+}]_i$, we used pipette solutions with K_2ATP or $MgATP$, respectively, as previously shown^{2,43}. Pipette solutions with K_2ATP (7 mM) showed a ~40% increase in g_j after 25 min of recording (Fig. 1f,g). Conversely, solutions with $MgATP$ (7 mM) showed a ~50% decrease in g_j after 25 min of recording (Fig. 1f,g). Therefore, inhibitory interneurons from the TRN showed a significant bi-directional Mg^{2+} -dependent modulation of g_j , in a similar manner as reported for excitatory neurons from the MesV⁴³.

E1 contains a pore-lining Mg^{2+} -sensitive domain

To locate the position of putative Mg^{2+} -sensitive domain/s in Cx36, we performed structure-function studies by assessing g_j in response to $[Mg^{2+}]_i$ in pairs of RIN cells expressing Cx36/Cx43 chimeras and mutants with single amino acid substitutions. We selected Cx43 because it shows a higher single channel conductance (γ_{open}) (~110 pS⁴⁷), a higher V_j -gating sensitivity and a lower sensitivity to changes in $[Mg^{2+}]_i$ ⁴³, relative to Cx36. Chimeras (CH) were generated by sequential exchange of corresponding domains of Cx36 and Cx43 using a modified version of the “sticky feet” protocol⁴⁸ (See Methods and Supplementary Figs. 2 and 3). We swapped selected domains at the expected interface between membrane and extracellular domains, and generated a total of sixteen chimeras from which eight formed junctional plaques (all chimeras were tagged with EGFP at the C-terminus (CT) and expressed in RIN cells) and only four (CH1-CH4) formed functional channels exhibiting electrical cell-cell coupling (Fig. 2). We studied sensitivity to $[Mg^{2+}]_i$ by measuring g_j at the beginning of the recording ($g_{j,initial}$) and the ratio of $g_{j,final}/g_{j,initial}$, where $g_{j,final}$ is the g_j value at the steady state level (after ~25 min), using pipette solutions with low or high free Mg^{2+} concentrations; $[Mg^{2+}]_p = 0.01$ or 5 mM. Cell pairs with approximately the same size of junctional plaques were used to study wild type and chimeric GJs. The Mg^{2+} -sensitivity of homotypic GJs formed by CH1 (see Supplementary Fig. 4 for amino acid sequence of functional chimeras), in which the NT and first transmembrane domain (M1) of Cx36 was replaced by those of Cx43, was similar to the Mg^{2+} -sensitivity of Cx36 (Fig. 3). Homotypic GJs formed by CH2 or CH3, in which E1 of Cx43 was replaced by E1 of Cx36, showed Mg^{2+} -sensitivity similar to that of Cx36 GJs (Fig. 3). GJs formed by CH4, in which only E2 of Cx43 was replaced by E2 of Cx36, showed no changes in sensitivity to Mg^{2+} and was similar to that of Cx43 GJs (Fig. 3). Altogether, results from Cx36/Cx43 chimeras indicate that E1 contains a Mg^{2+} -sensitive domain that can be transferred between Cxs, and that NT, M1 and E2 are not involved in Mg^{2+} -sensitivity.

D47 is critical for determining high sensitivity to $[Mg^{2+}]_i$

To locate region/s in E1 that may be responsible for the difference in Mg^{2+} -sensitivity between Cx36 and Cx43, we generated single amino acid substitutions in non-conserved charged residues of Cx36 and Cx43 (Supplementary Fig. 5). Mutation M52K and V54D in Cx36, and E62N in Cx43 had no effect on Mg^{2+} -sensitivity. In contrast, GJs formed of Cx36*D47G lost sensitivity to resting/initial $[Mg^{2+}]_i$, while GJs formed of Cx43*G46D

gained sensitivity to resting/initial $[Mg^{2+}]_i$ (Fig. 3). Position D47 in Cx36 corresponds to position G46 in Cx43. Moreover, GJs formed of CH3*D47G lost sensitivity to resting/initial $[Mg^{2+}]_i$ (Fig. 3). In summary, these data demonstrate that E1 contains a Mg^{2+} -sensitive domain in which the D47 residue is critical to determine the uniquely high sensitivity of Cx36 GJ channels to Mg^{2+} , and that insertion of this single residue in Cx43 confers high sensitivity to Mg^{2+} .

The γ_{open} of Cx36/Cx43 chimeras is not affected by $[Mg^{2+}]_i$

The γ_{open} of Cx36 GJ channels remains uncertain due to its very low conductance^{49,50}. For similar reasons, we were unable to examine with sufficient resolution the effects of $[Mg^{2+}]_i$ on single Cx36 GJ channels. However, the effect of $[Mg^{2+}]_i$ at the single channel level was amenable to analysis in Cx43-based chimeras and mutants, which exhibited γ_{open} s similar to that of Cx43 GJs. We found that γ_{open} of CH3 remained unchanged when $[Mg^{2+}]_p = 0.01$ and 5 mM (Fig. 4a,e). These results are in agreement with our hypothesis that $[Mg^{2+}]_i$ controls electrical transmission mostly via gating mechanisms, as we previously suggested using a stochastic 16-state of GJ channels⁴³. Furthermore, γ_{open} of homotypic CH3*D47G and CH4 GJs, both with low sensitivity to Mg^{2+} compared to that of CH3 GJs, was also similar to γ_{open} of Cx43 and remained unchanged in $[Mg^{2+}]_p = 0.01$ and 5 mM (Fig. 4b–c,e and Supplementary Fig. 6). In addition, γ_{open} of Cx43*G46D GJs remained close to that of Cx43 at high and low $[Mg^{2+}]_p$ (Fig. 4d–e). Homotypic GJs formed by CH3, CH3*D47G, CH4, and Cx43*G46D did not show I_j rectification at the single channel level. Thus, Mg^{2+} -dependent changes in g_j for these three chimeras and Cx43 most likely are defined by differences in Mg^{2+} binding affinity and its effects on gating, but not by changes in γ_{open} .

$[Mg^{2+}]_i$ affects g_j via gating mechanisms

CH3 channels possess the Mg^{2+} -sensitive E1 domain of Cx36 (Figs. 2 and 3) and the high γ_{open} is similar to that of Cx43 (Fig. 4), which allows for analysis of Mg^{2+} -dependent plasticity at the single channel level. We studied g_j and its dependence on V_j in pairs of weakly-coupled RIN cells expressing homotypic CH3 GJs. We measured $g_{j,ss}-V_j$ relationships using V_j ramps from 0 to +90 and –90 mV in amplitude and 30 s in duration (Fig. 5a, top trace). Under high $[Mg^{2+}]_p$, there was a relatively fast run-down of g_j in CH3 GJs, thus g_j-V_j plots from four consecutive measurements show different g_j s at the beginning of each ramp (Fig. 5a–c). The initial g_j was ~3.8 nS, corresponding to ~33 open CH3 GJ channels (Fig. 5a,c). Three minutes later, only one GJ channel was open during the fourth V_j ramp (red traces in Fig. 5a,c). To study the effects of Mg^{2+} occupancy inside the pore on V_j -gating, a transjunctional gradient of $[Mg^{2+}]_i$ was created by having different $[Mg^{2+}]_p$ (Fig. 5d); under these conditions relative positivity or negativity on the side with higher $[Mg^{2+}]_i$ should increase or reduce Mg^{2+} occupancy, respectively. The transjunctional asymmetry in $[Mg^{2+}]_i$ resulted in strong asymmetric $g_{j,ss}-V_j$ dependence measured using V_j ramps (Fig. 5e). At the single channel level, negative V_j steps applied in the cell with lower $[Mg^{2+}]_i$ facilitated closing events, while positive V_j steps facilitated opening events (Fig. 5f). The γ_{open} of CH3 GJ channels remained at ~115 pS regardless of the V_j polarity and Mg^{2+} occupancy (Fig. 5g–h). These results indicate that an increase in Mg^{2+} concentration inside the pore tends to close V_j -sensitive gates.

Transjunctional asymmetry of $[Mg^{2+}]_i$ induces rectification

To determine whether $[Mg^{2+}]_i$ affects γ_{open} of Cx36 GJ channels in a V_j -dependent manner, we examined the $g_{j,inst}-V_j$ relationship at different $[Mg^{2+}]_i$. The $g_{j,inst}-V_j$ dependence is relevant to the behavior of electrical synapses, because V_j generated in neurons arises mostly from action potentials with fast (milliseconds) oscillatory changes in the membrane potential. Instantaneous macroscopic I_{js} ($I_{j,inst}$) mainly reflect the dependence of γ_{open} on V_j in the absence of V_j -dependent gating. Thus, we measured steady-state and instantaneous g_j-V_j dependencies at different $[Mg^{2+}]_i$ by using different V_j protocols (Fig. 6a–b). We found that under high $[Mg^{2+}]_i$, the $g_{j,inst}$ (normalized to g_j value at zero V_j) of Cx36 GJs increased while the $g_{j,ss}$ decreased by increasing V_j s for both polarities (Fig. 6c, top panel). Low $[Mg^{2+}]_i$ fully eliminated or strongly reduced instantaneous and steady-state g_j dependencies on V_j (Fig. 6d, top panel). Moreover, transjunctional asymmetry in $[Mg^{2+}]_i$ induced asymmetric steady-state and instantaneous g_j-V_j dependencies (Fig. 6e, top panel). The effects of symmetric and asymmetric $[Mg^{2+}]_i$ on steady-state and instantaneous g_j-V_j dependencies were still present, albeit reduced, in GJs formed by Cx36*D47G (Fig. 6c–e, middle panels, & Fig. 6f), but absent for $g_{j,inst}-V_j$ dependence in GJs formed by CH3 (Fig. 6c–e, bottom panels). In addition, we found that the effects of $[Mg^{2+}]_i$ were eliminated in CH1 only for $g_{j,inst}-V_j$ but not for $g_{j,ss}-V_j$ dependencies (Supplementary Fig. 7), suggesting that residues in NT or M1 of Cx36 are necessary for the peculiar hyperbola-like $g_{j,inst}-V_j$ rectification. Altogether, these results suggest that $[Mg^{2+}]_i$ affects Cx36 GJ channels by: 1) gating through its binding in E1 and/or stabilizing a closed conformation of the channel; and 2) rectification of $I_{j,inst}$ depending on V_j (see Discussion).

Mg^{2+} -sensitive heterotypic GJs show asymmetric g_j-V_j relation

Heterotypic GJs formed by Cxs with highly different properties, such as Cx36 and Cx43, present a valuable tool for a high resolution analysis of the individual aHC properties. Our studies revealed that Cx36 does not form either JPs or functional coupling with Cx43, consistent with reports that neurons and astrocytes do not form Cx36/Cx43 heterotypic GJs⁵¹. We found that Cx36 or Cx43 were able to form functional heterotypic channels with chimeras that contain E2 of Cx36 or Cx43, respectively (Fig. 7). Thus, E2 determines incompatibility between Cx36 and Cx43. For heterotypic pairings, we used Cx36 and Cx43 tagged with CFP, while all chimeras were tagged with EGFP. This allowed us to detect junctional plaques with heterotypic GJs visible in two colors²⁸. In Cx43/CH3 heterotypic GJs, both aHCs have a similar unitary conductance ($\gamma_{open,H}$), but differential sensitivity to $[Mg^{2+}]_i$ (Figs. 3 and 4). Thus, this heterotypic configuration allows the study of Mg^{2+} -sensitivity in CH3 aHCs, and any detected asymmetry can be attributed to the difference in Mg^{2+} -sensitivity of aHCs but not $\gamma_{open,H}$. Indeed, heterotypic Cx43/CH3 GJs show marked asymmetric $g_{j,ss}-V_j$ dependence under symmetric high $[Mg^{2+}]_i$ (Fig. 8a). At $[Mg^{2+}]_p = 5$ mM, positive V_j ramps applied on the Cx43 side induced strong gating of the CH3 aHC, suggesting that CH3 aHCs have a negative gating polarity, as has been proposed for Cx43⁵². However, V_j -dependent gating of CH3 aHC at negative V_j s almost disappears under symmetric low $[Mg^{2+}]_i$ (Fig. 8b). At the single channel level, heterotypic Cx43/CH3 GJs showed asymmetric gating behavior (Fig. 8c). Negative V_j steps applied on the Cx43 side induced fast flickering of channels, while positive V_j steps induced channel closing (Fig. 8c).

Moreover, the asymmetric gating behavior of homotypic CH3 GJ channels under asymmetric $[Mg^{2+}]_i$ (Fig. 5c) can be replicated in heterotypic Cx43/CH3 channels under symmetric $[Mg^{2+}]_i$ (Fig. 8d). As expected from γ_{open} s of Cx43 and CH3 homotypic GJs, the γ_{open} of heterotypic Cx43/CH3 GJs is ~ 110 pS, and does not change under high or low $[Mg^{2+}]_i$. Thus, the macroscopic asymmetric $g_{j,ss}-V_j$ dependence shown in Fig. 8a can be explained by a Mg^{2+} -dependent modulation of gating mechanisms, in which negative potentials induce the transition of gates to a closed state, while positive potentials tend to reopen the gates. At low $[Mg^{2+}]_i$, most of the V_j -dependent gating is lost (Fig. 8b), suggesting that Mg^{2+} is necessary for V_j -sensitive gating. Furthermore, we studied $g_{j,ss}-V_j$ dependence of Cx43/CH3 GJs under asymmetric $[Mg^{2+}]_i$ (Fig. 8e,f). These experiments revealed that the direction of the Mg^{2+} gradient is important; the $g_{j,ss}-V_j$ asymmetry is strengthened when the Cx43 side has higher $[Mg^{2+}]_i$ (Fig. 8e) or reduced when the Cx43 side has lower $[Mg^{2+}]_i$ (Fig. 8f). These results strongly support the hypothesis that the site of Mg^{2+} interaction in CH3 aHC is located within the pore, and that high $[Mg^{2+}]_i$ inside the pore increases V_j -sensitive gating.

We studied $g_{j,ss}-V_j$ and $g_{j,inst}-V_j$ dependencies and sensitivity to $[Mg^{2+}]_i$ of Cx36 aHC in Cx36/CH4 heterotypic GJs. This heterotypic configuration allows for a higher resolution analysis of Mg^{2+} -sensitivity and of V_j -gating of Cx36 aHCs; in Cx36/CH4 GJs almost all V_j drops across the Cx36 aHCs due to a ~ 15 fold lower $\gamma_{open,H}$ than in CH4⁵³, making CH4 aHC virtually insensitive to V_j . We found that under high symmetric $[Mg^{2+}]_p$ (5 mM), $g_{j,inst}$ (normalized to g_j value at zero V_j) of heterotypic Cx36/CH4 GJs increased for both polarities of V_j (Fig. 9a, bottom), while $g_{j,ss}-V_j$ showed a marked asymmetric dependence (Fig. 9a, top). Interestingly, $g_{j,inst}-V_j$ dependence of heterotypic Cx36/CH4 GJs becomes less symmetric at low $[Mg^{2+}]_p$ (Fig. 9b, bottom), in which $g_{j,inst}$ increased only at relative negativity on the Cx36 side. The asymmetric $g_{j,ss}-V_j$ dependence almost disappears under low $[Mg^{2+}]_p$ (0.01 mM, Fig. 9b, top) due to a reduction in V_j -sensitivity, indicating that most of the asymmetry is due to the Mg^{2+} -sensitivity of Cx36 aHC. In order to study the mechanism of $I_{j,inst}-V_j$ rectification of the Cx36 aHC in more detail, we simulated $g_{j,inst}-V_j$ dependence curves that fit our experimental data using a stochastic four state model (S4SM) of GJ channels⁵⁴. $g_{j,inst}-V_j$ relationships of the Cx36 homotypic and Cx36/CH4 heterotypic GJs were simulated using a hyperbolic equation describing the Cx36 aHC conductance: $\gamma_{open,H} = \gamma_{open,H,0} * (e^{(V_H/r_H)} + e^{(-V_H/r_{Mg})})/2$, where $\gamma_{open,H,0}$ is $\gamma_{open,H}$ at $V_H = 0$, V_H is voltage across aHC, r_H and r_{Mg} are Mg^{2+} -independent and Mg^{2+} -dependent rectification coefficients of aHC, respectively. The CH4 aHC conductance was described using a single exponential equation: $\gamma_{open,H} = \gamma_{open,H,0} * e^{(V_H/r_H)}$. The simulated $g_{j,inst}-V_j$ curves for Cx36 (pink) and CH4 (purple) aHCs produced curves with good fit (grey) for steady-state and instantaneous g_j-V_j dependence of experimental data from heterotypic Cx36/CH4 GJs at low and high symmetric $[Mg^{2+}]_i$ (Fig. 9a–b). The same hyperbolic equation describing $\gamma_{open,H}$ of Cx36 and similar rectification values used in simulation of heterotypic Cx36/CH4 GJs were also used to simulate experimental data for homotypic Cx36 GJs at high and low $[Mg^{2+}]_i$ (Fig. 9c–d). All values of rectification and gating parameters are presented in Supplementary Table 1.

Discussion

Electrical synapses are known to function throughout the mammalian CNS, and Cx36 expression is necessary to produce robust neuronal coupling in many brain areas³⁵. We recently showed Mg²⁺-dependent modulation of signal transfer at electrical synapses between excitatory MesV neurons in the midbrain and that this [Mg²⁺]_i effect was similar to that observed in heterologous expression systems⁴³.

Here, we demonstrated that electrical synapses formed by Cx36 GJs between GABAergic interneurons in the TRN also show Mg²⁺-dependent synaptic plasticity, and that the ratio between the total intracellular ATP and Mg²⁺ contributes to regulation of electrical coupling (Fig. 1). Although the magnitude of changes in g_j between TRN (Fig. 1) and MesV⁴³ neurons were significant (~30–40%), they were smaller than those observed in RIN cells expressing Cx36. This distinction may be explained by differences in the initial [Mg²⁺]_i and other divalent cations as well as the concentration of ATP and phosphocreatine, that exert a Mg²⁺ buffering capacity, and the location of JPs with respect to patch pipette attachment at the soma. Despite these differences, the magnitude of g_j changes is comparable to that of previous reports on long-term depression or potentiation of neuronal coupling^{40,42}. Taken together, these results support the hypothesis that Mg²⁺-dependent synaptic plasticity of Cx36-containing electrical synapses is neuronal-type independent and is a common mechanism that affects the strength of neuronal electrical coupling in the CNS.

We recently suggested that Mg²⁺ exerts its effects on g_j of Cx36 GJs via interaction with a domain in the channel lumen⁴³. This interaction may affect V_j-sensitive gates by modulating their sensitivity to voltage and stabilizing a closed state conformation⁴³. Previously, we showed that sensitivity to high [Mg²⁺]_i is similar in wild type Cx36 and Cx43, and tagged with fluorescent proteins⁴³. Here, using color variants of GFP tagged to Cx36/Cx43 chimeras and mutants, we demonstrate that E1 of Cx36 contains a Mg²⁺-sensitive domain and that it can be transferred to Cx43 (Fig. 3). In addition, single amino acid substitutions targeted to E1 of Cx36 and Cx43 revealed that residues in E1 are indeed responsible for the sensitivity to Mg²⁺ and that particularly D47 is critical for high Mg²⁺-sensitivity in Cx36 GJs (Fig. 3). Interestingly, the G46D mutation in Cx43 (corresponding location of D47 in Cx36) was sufficient to significantly increase sensitivity to Mg²⁺ in Cx43 (Fig. 3). Furthermore, as predicted from the crystal structure of Cx26⁵⁵, the side chains of the residue D47 in GJs formed by Cx36 face the pore, form a negatively-charged hexameric ring and contribute significantly to the negative surface potential of the pore (Fig. 10a–c), supporting the view that Mg²⁺ interacts with a pore-lining domain located in E1 and that residue D47 provides strong electro negative surface potential, which may increase Mg²⁺ occupancy. It is noteworthy that recent quantum chemistry studies in Cx26 structure have proposed that Ca²⁺ may directly interact with E47 (E49 in Cx36) to induce closure of the channel by a gating mechanism⁵⁶. Other intracellular cations, such as spermine, have been shown to affect V_j-dependent gating mechanisms by interacting with charged residues located in the N-terminus⁵⁷. In addition, spermine can influence the Mg-ATP binding affinity², and therefore modulate its action on g_j and gating.

Single channel analysis of Cx43-based chimeras and mutants (CH2, CH3, CH4, and Cx43*G46D) showed that γ_{open} is not affected by $[\text{Mg}^{2+}]_i$ (Fig. 4), and a long-lived residual state is absent, indicating that the fast gating mechanism is inhibited most likely due to C-terminus tagging by fluorescent proteins⁵⁸. The latter can reduce $g_{j,ss}$ dependence on V_j in Cx43/CH3 heterotypic GJs (Fig. 8), but should not influence $g_{j,ss}$ - V_j dependence of Cx36/CH4 GJs (Fig. 9) due to a significant difference in $\gamma_{\text{open,H}}$ of Cx36 and CH4 aHCs, making CH4 aHC unlikely to be gated by V_j . In addition, γ_{open} and V_j -sensitive gating records under transjunctional asymmetry in $[\text{Mg}^{2+}]_i$ allowed us to conclude that changes in $[\text{Mg}^{2+}]$ inside the pore are necessary for the observed asymmetry in the $g_{j,ss}$ - V_j relationship of CH3 GJs (Figs. 5d–f and 8e–f).

Cx36 is not compatible to dock with Cx43, but is compatible with CH2 and CH4. Cx43 is compatible with CH1 and CH3 but not with CH2 and CH4 (Fig. 7). These data suggest that E2 is an important structural determinant for the incompatibility between Cx36 and Cx43, consistent with reports showing the key role E2 plays in determining compatibility between different Cxs^{59,60}. Cx43/CH3 heterotypic GJs showed a marked asymmetry in the g_j - V_j relationship, and this asymmetry was dependent on $[\text{Mg}^{2+}]_i$ (Fig. 8a–b). CH3 GJs exhibited similar sensitivity to Mg^{2+} compared to that of Cx36 (Fig. 3), while its γ_{open} is >15 fold higher than that of Cx36. Macroscopic and single channel recordings of Cx43/CH3 GJs (Fig. 8a,d) under high $[\text{Mg}^{2+}]_i$ show significant V_j -gating asymmetry with pronounced sensitivity to V_j at relative negativity on the CH3 side. The dependence of V_j -gating asymmetry on the Mg^{2+} gradient in Cx43/CH3 heterotypic GJs (Fig. 8e–f) demonstrates that asymmetric gating is determined not only by $[\text{Mg}^{2+}]_i$ concentration inside the pore, but also by its influence on V_j -sensitivity. When $[\text{Mg}^{2+}]_i$ is higher on the Cx43 side, the $g_{j,ss}$ - V_j asymmetry is enhanced compared to that under high symmetric $[\text{Mg}^{2+}]_i$. These effects are presumably due to increased V_j -gating and Mg^{2+} occupancy during positive V_j s applied on the Cx43 side, and decreased V_j -gating and Mg^{2+} occupancy during negative V_j s applied on the Cx43 side (Fig. 8e). Conversely, when $[\text{Mg}^{2+}]_i$ is lower on the Cx43 side, the g_j - V_j asymmetry is reduced and opposite compared to the one at high symmetric $[\text{Mg}^{2+}]_i$ (Fig. 8f). Consistent with our data, a three-state model of Mg^{2+} -dependent gating of Cx37 HCs, also suggests the stabilization of a closed state by Mg^{2+} binding⁶¹.

We found a unique $g_{j,\text{inst}}$ - V_j relationship dependence on $[\text{Mg}^{2+}]_i$ of Cx36 GJ channels. Reported and preliminary data show that all examined Cxs with the exception of Cx36 demonstrate no or minimal decay of $g_{j,\text{inst}}$ dependence on V_j for both V_j polarities⁵². The symmetric increase in $g_{j,\text{inst}}$ at high V_j s for Cx36 was previously reported in the oocyte expression system at normal/resting $[\text{Mg}^{2+}]_i$ ⁶². Here, we show that $g_{j,\text{inst}}$ s at high $[\text{Mg}^{2+}]_i$ increases ~1.4 fold at $V_j = \pm 100$ mV, and that this increase disappears under low $[\text{Mg}^{2+}]_i$ (Fig. 6c–d). All our attempts to replicate the observed $g_{j,\text{inst}}$ - V_j dependence at high $[\text{Mg}^{2+}]_i$ using a one-dimensional Poisson-Nernst-Planck (PNP) model⁶³ were unsuccessful. Studies of heterotypic CH4/Cx36 GJs show that $g_{j,\text{inst}}$ increased for both polarities of V_j at high $[\text{Mg}^{2+}]_i$ (Fig. 9a) and only at relative negativity of V_j at low $[\text{Mg}^{2+}]_i$ on the Cx36 side (Fig. 9b). Thus, the $g_{j,\text{inst}}$ - V_j relationship of Cx36 aHC transforms from hyperbola-like to exponential-like when $[\text{Mg}^{2+}]_p$ decreases from 5 to 0.01 mM (Fig. 9a–b). An approximately 15-fold difference in $\gamma_{\text{open,H}}$ between Cx36 and CH4 aHCs allows us to assume that

measured $g_{j,\text{inst}}-V_j$ rectification in Cx36/CH4 GJs can be attributed solely to the Cx36 aHC. These data suggest that $g_{j,\text{inst}}-V_j$ rectification of Cx36 aHC contains two exponential-like components in opposite orientation with respect to V_j polarity, defined by: 1) asymmetry of fixed charges inside the Cx36 aHC pore, as described by PNP equations⁶³; and 2) $[\text{Mg}^{2+}]_i$. Fig. 10d (top) shows a family of simulated $g_{j,\text{inst}}-V_j$ plots for Cx36 aHCs using S4SM (details in the Results section), in which the rectification coefficient, r_H , was constant and equal to 90 mV, and the Mg^{2+} -dependent rectification coefficient, r_{Mg} , changed from ~200 to 80 mV when $[\text{Mg}^{2+}]_i$ increased from ~0.01 to 5 mM. Fig. 10d (bottom) shows simulated $g_{j,\text{inst}}-V_j$ plots of homotypic Cx36 GJs using the same parameters as for Cx36 aHCs. Thus, Mg^{2+} -dependent rectification can explain the transformation of $g_{j,\text{inst}}-V_j$ dependence observed in heterotypic Cx36/CH4 (Fig. 9a–b) and homotypic Cx36 (Fig. 9c–d) GJs. Hyperbola-like conductance-voltage rectification has also been shown in a solid back-to-back p-n junction⁶⁴, but applicability of such junctions to GJ channels remains unclear. The $g_{j,\text{inst}}-V_j$ rectification was not observed under high or low $[\text{Mg}^{2+}]_i$ in CH1 GJs (Supplementary Fig. 7), suggesting that residues in the NT-M1 region of the Cx36 protein are necessary for instantaneous rectification.

To our knowledge, molecular mechanisms of electrical rectification in GJs have been examined only in heterotypic GJs. In this regard, two mechanisms have been proposed: differences in fast V_j -dependent gating and gating polarity of aHCs of heterotypic GJs^{65,66}; and/or rectification of the single channel conductance resulting from an asymmetry in the number and position of charged residues inside the channel pore of heterotypic GJs⁶⁷. Thus, we propose that transjunctional asymmetry in $[\text{Mg}^{2+}]_i$ can serve as a novel mechanism for electrical rectification in homotypic GJs (Fig. 6e). It is important to note that the degree of rectification in electrical synapses has been proposed to affect the dynamic output of neuronal networks⁶⁸, and therefore this novel instantaneous Mg^{2+} -dependent rectification could be important to explain the phenomenon of switching between firing states and changes in the output of neuronal networks during different metabolic states where $[\text{Mg}^{2+}]_i$ is affected. Taken together, these findings suggest that changes in $[\text{Mg}^{2+}]_i$ may be sufficient to induce plasticity of Cx36-based electrical synaptic transmission.

Methods

Generation of chimeras and mutants

All chimeras were generated using a modified version of the “sticky feet”-directed mutagenesis protocol⁴⁸. Briefly, long PCR oligonucleotide primers that share a complementary sequence were used as forward or reverse primers to isolate fragments with complementary ends of two different genes (1st PCR step). Subsequently, these long DNA fragments were used as primer DNAs to produce chimeric fragments from two different genes (2nd PCR step). This protocol is illustrated in Supplementary Fig. 2. A total of 22 different DNA fragments with complementary ends (FX-1 and FX-2) were generated in order to produce 14 different chimeric fragments (FX) (Supplementary Fig. 3). Two additional chimeric fragments (F12 and F16) were generated by restriction enzyme subcloning (Supplementary Fig. 3). A list of all primer sequences and restriction enzymes used in the generation of each DNA fragment is provided in Supplementary Table 2. Design

of primers was assisted by Clone Manager Professional 9 (Sci-Ed software, NC, USA). Platinum PCR SuperMix High Fidelity (Life Technologies, NY, USA) were used for all PCRs. PCR products were separated by acrylamide gel electrophoresis and isolated with a gel extraction kit (Quiagen). All restriction enzymes were purchased from New England Biolabs. Amino acid substitutions in Cx36 and Cx43 were introduced using the Quickchange Multi Site-directed Mutagenesis Kit (Agilent, TX, USA) or ordered from Genscript (New Jersey, USA) using the site-directed mutagenesis service. Chimeras and mutant fragments were subcloned into pEGFP-N1 (Clontech, CA, USA). All plasmid transfections were performed with Lipofectamine 2000 (Life Technologies, NY USA).

Cell lines and culture conditions

Experiments were performed in RIN cells (rat beta-cell insulinoma, ATCC CRL-2057) transfected with Cx36, Cx43, chimeras or mutants fused with colour variants of green fluorescent proteins (EGFP or CFP) attached to the CT. All experiments were performed with stable cell lines to minimize variability. All cell cultures were grown in RPMI 1640, with L-glutamine, supplemented with 8% fetal calf serum, 100 µg per ml streptomycin and 100 units per ml penicillin, and maintained in a CO₂ incubator (37 °C and 5% CO₂).

In vitro electrophysiology

Electrophysiological recordings were performed in cell cultures grown on glass coverslips and submerged on an experimental chamber mounted on the stage of an inverted IX70 microscope (Olympus) equipped with a fluorescence imaging system. Extracellular solution contained (in mM): 140 NaCl, 4 KCl, 2 CaCl₂, 1 MgCl₂, 2 CsCl, 1 BaCl₂, 5 glucose, 2 pyruvate, and 5 HEPES (pH 7.4 adjusted with NaOH). Standard pipette solution contained (in mM): 130 CsCl, 10 NaAsp, 1 MgCl₂, 0.26 CaCl₂, 2 EGTA, and 5 HEPES (pH 7.2 adjusted with CsOH). Resistance of recording pipettes was in the order of 3–5 MΩ. We used either EDTA or MgCl₂ and the web-based Maxchelator software to adjust and calculate free Mg²⁺ concentration in the pipette solutions. Junctional conductance (g_j) was measured using two EPC-8 patch clamp amplifiers (HEKA); briefly, a transjunctional voltage (V_j) was generated by modifying voltage in cell-1 (V_1) and keeping the voltage in cell-2 (V_2) constant ($V_j = V_1$). Application of V_j induced a transjunctional current (I_j) of opposite polarity to V_j ($I_j = -I_2$, and $g_j = I_j/V_j$). Signals were digitized using an A/D converter (Axon instruments) and data were acquired and analyzed using custom-made software.

Brain-slice preparation and electrophysiology

A minimal number of animals were sacrificed in accordance with the National Institute of Health *Guide for the Care and Use of Laboratory Animals*, and with the provisions of the Institutional Animal Care and Use Committee of the Marine Biological Laboratory. Horizontal brain slices (300-µm thick) were prepared from the BAC transgenic mouse line Tg(*Gjd2-EGFP*)JM16Gsat/Mmucd⁴⁴, in which the expression of EGFP reporter gene is driven by the activity of the Cx36 promoter. Male or female mice age between P5 and P15 were used. Brain slices were obtained using a chilled VT1200 blade vibrating microtome (Leica Biosystems, IL, USA) and sliced in cold sucrose solution containing (in mM): 238 sucrose, 2.7 KCl, 1.25 KH₂PO₄, 26 NaHCO₃, 11 Glucose, 2 CaCl₂, and 2 MgSO₄. Brain

slices were transferred to an incubation chamber with extracellular recording solution and incubated for 20 min at 37 °C. The extracellular recording solution contained (in mM): 124 NaCl, 2.7 KCl, 1.25 KH₂PO₄, 26 NaHCO₃, 10 Glucose, 2 CaCl₂, and 2 MgSO₄. The incubation chamber was then kept at room temperature for 30–40 min prior to electrophysiology. Brain slices were then transferred to a low-noise RC-27LD recording chamber (Warner Instruments, Hamden, CT) mounted on an Axio Examiner A1 microscope (Zeiss, Thornwood, NY) equipped with an Orca-R2 digital camera (Hamamatsu, Bridgewater, NJ) for infrared differential interference contrast (IR-DIC) and fluorescence imaging. Extracellular recording solution was continuously exchanged (~2 ml per min) at room temperature in the chamber by a gravity feed perfusion system. All sucrose and extracellular solutions were constantly bubbled and saturated with carbogen (95% oxygen/5% CO₂) throughout the slice procedure and electrophysiology experiments. TRN neurons were identified based on characteristic location, cell shape and electrophysiological properties⁴⁵. A standard pipette solution contained (in mM): 120 K-Gluconate, 20 KCl, 2 MgCl₂, 0.2 EGTA, and 10 HEPES (pH 7.2 adjusted with KOH). Resistance of recording pipettes was on the order of 6–10 MΩ. We used K₂ATP or MgATP to decrease or increase, respectively, free Mg²⁺ concentration in the pipette solutions^{2,43}. Changes in membrane voltage and current were measured using two separate Axopatch 200B amplifiers, digitized using a Digidata 1440A, and acquired and analyzed using pClamp 10 software (Molecular Devices, Sunnyvale, CA). The g_j was measured and calculated as explained for the in vitro electrophysiology (see above).

Confocal microscopy and fluorescence imaging

Fluorescence signals from EGFP expression in acute TRN brain slices were acquired using a LSM-780 Quasar confocal system configured on an inverted Observer Z1 microscope. Imaging during electrophysiology studies was conducted using an Axio Examiner A1 microscope (Zeiss, Oberkochen, Germany) equipped with an Orca-R2 digital camera (Hamamatsu Corp., Bridgewater, NJ). Image acquisition and processing were performed using ZEN software (Zeiss, Oberkochen, Germany). For in vitro studies, fluorescence signals from EGFP or CFP were acquired using an IX70 microscope (Olympus, USA) equipped with an ORCA-R2 digital camera (Hamamatsu Corp., Bridgewater, NJ). Image acquisition and processing were performed using UltraVIEW software (Perkin Elmer Life Sciences, Boston, MA).

Homology models and electrostatic surface potential

Structural homology models of Cx36 and Cx36*D47G were built using the known three-dimensional structure of Cx26 as a template⁵⁵. The corresponding Cx26 cytoplasmic loop and C-terminus domains of Cx36 were deleted, and the target-template alignment was selected by hand, scoring a sequence identity of 47%. Based on this alignment, 200 models were generated by means of the MODELLER program and the best model was selected according to the DOPE score⁶⁹. The electrostatic potential on the solvent accessible surface (surface potential) of the structural homology models was estimated using DELPHI, which provides finite difference solutions to the Poisson-Boltzmann equation⁷⁰. We chose to display surface potentials according to the electrostatic potential found at the solvent accessible surface instead of the atomic surface charges used in the original Cx26 crystal

structure article⁵⁵. This method takes in consideration an average of all surrounding atomic surface charges and displays less extreme values of electrostatic surface potential. Default dielectric constants of 2.0 for interior (protein) and 80.0 for exterior (solvent) regions were used.

Data analysis

The analysis and statistics were performed using SigmaPlot v10 (Systat Software Inc, Chicago, IL) and pClamp 10 (Molecular Devices, Sunnyvale, CA). Averaged data are reported as the means \pm s.e.m. Means for each group were compared using an unpaired student's t-test.

Supplementary Material

Refer to Web version on PubMed Central for supplementary material.

Acknowledgments

We thank Michael V.L. Bennett, Vytautas K. Verselis and Thaddeus A. Bargiello for helpful comments and discussions. We thank Nerijus Paulauskas for assistance with S4SM, and Angele Bukauskiene and Alius Dicpinigaitis for excellent technical assistance. We thank Jim McIlvain and Elizabeth Dille from Zeiss for assistance with confocal imaging. Nicolás Palacios-Prado is a Howard Hughes Medical Institute International Student Research Fellow. This work was supported by the Grass Foundation with a Grass Fellowship to N.P.-P., by a grant from the Canadian Institute of Health Research to J.I.N, and by the National Institute of Health grant R01NS 072238 to F.F.B.

References

1. Masuda T, Dobson GP, Veech RL. The Gibbs-Donnan near-equilibrium system of heart. *J. Biol. Chem.* 1990; 265:20321–20334. [PubMed: 2147022]
2. Luthi D, Gunzel D, McGuigan JA. Mg-ATP binding: its modification by spermine, the relevance to cytosolic Mg²⁺ buffering, changes in the intracellular ionized Mg²⁺ concentration and the estimation of Mg²⁺ by 31P-NMR. *Exp. Physiol.* 1999; 84:231–252. [PubMed: 10226168]
3. Taylor JS, et al. Free magnesium levels in normal human brain and brain tumors: 31P chemical-shift imaging measurements at 1.5 T. *Proc. Natl. Acad. Sci. U. S. A.* 1991; 88:6810–6814. [PubMed: 1650484]
4. Chen C, Nakatani K, Koutalos Y. Free magnesium concentration in salamander photoreceptor outer segments. *J. Physiol.* 2003; 553:125–135. [PubMed: 14500766]
5. Henrich M, Buckler KJ. Effects of anoxia, aglycemia, and acidosis on cytosolic Mg²⁺, ATP, and pH in rat sensory neurons. *Am. J. Physiol. Cell. Physiol.* 2008; 294:280–294.
6. Kato H, Gotoh H, Kajikawa M, Suto K. Depolarization triggers intracellular magnesium surge in cultured dorsal root ganglion neurons. *Brain Res.* 1998; 779:329–333. [PubMed: 9473713]
7. Cheng C, Reynolds IJ. Subcellular localization of glutamate-stimulated intracellular magnesium concentration changes in cultured rat forebrain neurons using confocal microscopy. *Neuroscience.* 2000; 95:973–979. [PubMed: 10682704]
8. Shindo Y, Fujimoto A, Hotta K, Suzuki K, Oka K. Glutamate-induced calcium increase mediates magnesium release from mitochondria in rat hippocampal neurons. *J. Neurosci. Res.* 2010; 88:3125–3132. [PubMed: 20740499]
9. Yamanaka R, Shindo Y, Hotta K, Suzuki K, Oka K. NO/cGMP/PKG signaling pathway induces magnesium release mediated by mitoKATP channel opening in rat hippocampal neurons. *FEBS Lett.* 2013; 587:2643–2648. [PubMed: 23831575]
10. Dworak M, McCarley RW, Kim T, Kalinchuk AV, Basheer R. Sleep and brain energy levels: ATP changes during sleep. *J. Neurosci.* 2010; 30:9007–9016. [PubMed: 20592221]

11. Ainscow EK, Mirshamsi S, Tang T, Ashford ML, Rutter GA. Dynamic imaging of free cytosolic ATP concentration during fuel sensing by rat hypothalamic neurones: evidence for ATP-independent control of ATP-sensitive K(+) channels. *J. Physiol.* 2002; 544:429–445. [PubMed: 12381816]
12. Sims NR, Muyderman H. Mitochondria, oxidative metabolism and cell death in stroke. *Biochim. Biophys. Acta.* 2010; 1802:80–91. [PubMed: 19751827]
13. Williams GD, Smith MB. Application of the accurate assessment of intracellular magnesium and pH from the 31P shifts of ATP to cerebral hypoxia-ischemia in neonatal rat. *Mag. Res. Med.* 1995; 33:853–857.
14. Zhang J, et al. Hypoxia induces an increase in intracellular magnesium via transient receptor potential melastatin 7 (TRPM7) channels in rat hippocampal neurons in vitro. *J. Biol. Chem.* 2011; 286:20194–20207. [PubMed: 21487014]
15. Hinsberger AD, et al. Magnetic resonance imaging volumetric and phosphorus 31 magnetic resonance spectroscopy measurements in schizophrenia. *J. Psychiatry Neurosci.* 1997; 22:111–117. [PubMed: 9074305]
16. Cernak I, Radosevic P, Malicevic Z, Savic J. Experimental magnesium depletion in adult rabbits caused by blast overpressure. *Magnes. Res.* 1995; 8:249–259. [PubMed: 8845290]
17. Suzuki M, et al. Decrease in cerebral free magnesium concentration following closed head injury and effects of VA-045 in rats. *Gen. Pharmacol.* 1997; 28:119–121. [PubMed: 9112087]
18. Oyanagi K, et al. Magnesium deficiency over generations in rats with special references to the pathogenesis of the Parkinsonism-dementia complex and amyotrophic lateral sclerosis of Guam. *Neuropathology.* 2006; 26:115–128. [PubMed: 16708544]
19. Andradi E, Igaz S, Molnar Z, Mako S. Disturbances of magnesium concentrations in various brain areas in Alzheimer's disease. *Magnes. Res.* 2000; 13:189–196. [PubMed: 11008926]
20. Stelmasiak Z, Solski J, Jakubowska B. Magnesium concentration in plasma and erythrocytes in MS. *Acta Neurol. Scand.* 1995; 92:109–111. [PubMed: 7572055]
21. Yasui M, Yase Y, Kihira T, Adachi K, Suzuki Y. Magnesium and calcium contents in CNS tissues of amyotrophic lateral sclerosis patients from the Kii peninsula, Japan. *Euro. Neurol.* 1992; 32:95–98.
22. Lodi R, et al. Deficit of brain and skeletal muscle bioenergetics and low brain magnesium in juvenile migraine: an in vivo 31P magnetic resonance spectroscopy interictal study. *Pediatr. Res.* 1997; 42:866–871. [PubMed: 9396571]
23. Barbiroli B, et al. Low brain intracellular free magnesium in mitochondrial cytopathies. *J. Cereb. Blood. Flow. Metab.* 1999; 19:528–532. [PubMed: 10326720]
24. Bennett MV, Zukin RS. Electrical coupling and neuronal synchronization in the Mammalian brain. *Neuron.* 2004; 41:495–511. [PubMed: 14980200]
25. Bissiere S, Zelikowsky M, Ponnusamy R, Jacobs NS, Blair HT, Fanselow MS. Electrical synapses control hippocampal contributions to fear learning and memory. *Science.* 2011; 331:87–91. [PubMed: 21212357]
26. Yaksi E, Wilson RI. Electrical coupling between olfactory glomeruli. *Neuron.* 2010; 67:1034–1047. [PubMed: 20869599]
27. Bukauskas FF, Weingart R. Voltage-dependent gating of single gap junction channels in an insect cell line. *Biophys J.* 1994; 67:613–625. [PubMed: 7524710]
28. Palacios-Prado N, Bukauskas FF. Heterotypic gap junction channels as voltage-sensitive valves for intercellular signaling. *Proc. Natl. Acad. Sci. U. S. A.* 2009; 106:14855–14860. [PubMed: 19706392]
29. Palacios-Prado N, Bukauskas FF. Modulation of metabolic communication through gap junction channels by transjunctional voltage; synergistic and antagonistic effects of gating and ionophoresis. *Biochim. Biophys. Acta.* 2012; 1818:1884–94. [PubMed: 21930112]
30. Furshpan EJ, Potter DD. Transmission at the giant motor synapses of the crayfish. *J. Physiol.* 1959; 145:289–325. [PubMed: 13642302]
31. Auerbach AA, Bennett MVL. A rectifying electrotonic synapse in the central nervous system of a vertebrate. *J. Gen. Physiol.* 1969; 53:211–237. [PubMed: 4303657]

32. Phelan P, et al. Molecular mechanism of rectification at identified electrical synapses in the *Drosophila* giant fiber system. *Curr. Biol.* 2008; 18:1955–1960. [PubMed: 19084406]
33. Rash JE, et al. Molecular and functional asymmetry at a vertebrate electrical synapse. *Neuron.* 2013; 79:957–969. [PubMed: 24012008]
34. Sohl G, Maxeiner S, Willecke K. Expression and functions of neuronal gap junctions. *Nat. Rev. Neurosci.* 2005; 6:191–200. [PubMed: 15738956]
35. Connors BW, Long MA. Electrical synapses in the mammalian brain. *Annu. Rev. Neurosci.* 2004; 27:393–418. [PubMed: 15217338]
36. Ouyang X, Winbow VM, Patel LS, Burr GS, Mitchell CK, O'Brien J. Protein kinase A mediates regulation of gap junctions containing connexin35 through a complex pathway. *Brain Res. Mol. Brain. Res.* 2005; 135:1–11. [PubMed: 15857663]
37. Alev C, et al. The neuronal connexin36 interacts with and is phosphorylated by CaMKII in a way similar to CaMKII interaction with glutamate receptors. *Proc. Natl. Acad. Sci. U. S. A.* 2008; 105:20964–20969. [PubMed: 19095792]
38. González-Nieto D, et al. Regulation of neuronal connexin-36 channels by pH. *Proc. Natl. Acad. Sci. U. S. A.* 2008; 105:17169–17174. [PubMed: 18957549]
39. Marandykina A, Palacios-Prado N, Rimkut L, Skeberdis VA, Bukauskas FF. Regulation of Connexin-36 Gap Junction Channels by n-Alkanols and Arachidonic Acid. *J. Physiol.* 2013; 591:2087–2101. [PubMed: 23420660]
40. Haas JS, Zavala B, Landisman CE. Activity-dependent long-term depression of electrical synapses. *Science.* 2011; 334:389–393. [PubMed: 22021860]
41. Pereda AE, et al. Ca²⁺/calmodulin-dependent kinase II mediates simultaneous enhancement of gap-junctional conductance and glutamatergic transmission. *Proc. Natl. Acad. Sci. U. S. A.* 1998; 95:13272–13277. [PubMed: 9789078]
42. Cachope R, Mackie K, Triller A, O'Brien J, Pereda AE. Potentiation of electrical and chemical synaptic transmission mediated by endocannabinoids. *Neuron.* 2007; 56:1034–1047. [PubMed: 18093525]
43. Palacios-Prado N, et al. Intracellular Magnesium-Dependent Modulation of Gap Junction Channels Formed by Neuronal connexin36. *J. Neurosci.* 2013; 33:4741–4753. [PubMed: 23486946]
44. Gong S, et al. A gene expression atlas of the central nervous system based on bacterial artificial chromosomes. *Nature.* 2003; 425:917–925. [PubMed: 14586460]
45. Landisman CE, Long MA, Beierlein M, Deans MR, Paul DL, Connors BW. Electrical synapses in the thalamic reticular nucleus. *J. Neurosci.* 2002; 22:1002–1009. [PubMed: 11826128]
46. Pinault D. The thalamic reticular nucleus: structure, function and concept. *Brain Res. Brain. Res. Rev.* 2004; 46:1–31. [PubMed: 15297152]
47. Bukauskas FF, et al. Clustering of connexin 43-enhanced green fluorescent protein gap junction channels and functional coupling in living cells. *Proc. Natl. Acad. Sci. U. S. A.* 2000; 97:2556–2561. [PubMed: 10706639]
48. Clackson T, Winter G. 'Sticky feet'-directed mutagenesis and its application to swapping antibody domains. *Nucleic Acids Res.* 1989; 17:10163–10170. [PubMed: 2690014]
49. Srinivas M, et al. Functional properties of channels formed by the neuronal gap junction protein connexin36. *J. Neurosci.* 1999; 19:9848–9855. [PubMed: 10559394]
50. Moreno AP, Berthoud VM, Perez-Palacios G, Perez-Armendariz EM. Biophysical evidence that connexin-36 forms functional gap junction channels between pancreatic mouse beta-cells. *Am. J. Physiol. Endocrinol. Metab.* 2005; 288:948–956.
51. Rash JE, Yasumura T, Dudek FE, Nagy JI. Cell-specific expression of connexins and evidence of restricted gap junctional coupling between glial cells and between neurons. *J. Neurosci.* 2001; 21:1983–2000. [PubMed: 11245683]
52. Bukauskas FF, Verselis VK. Gap junction channel gating. *Biochim. Biophys. Acta.* 2004; 1662:42–60. [PubMed: 15033578]
53. Palacios-Prado N, Briggs SW, Skeberdis VA, Pranevicius M, Bennett MV, Bukauskas FF. pH-dependent modulation of voltage gating in connexin45 homotypic and connexin45/connexin43 heterotypic gap junctions. *Proc. Natl. Acad. Sci. U. S. A.* 2010; 107:9897–9902. [PubMed: 20445098]

54. Paulauskas N, Pranevicius M, Pranevicius H, Bukauskas FF. A stochastic four-state model of contingent gating of gap junction channels containing two "fast" gates sensitive to transjunctional voltage. *Biophys. J.* 2009; 96:3936–3948. [PubMed: 19450466]
55. Maeda S, et al. Structure of the connexin 26 gap junction channel at 3.5 Å resolution. *Nature.* 2009; 458:597–602. [PubMed: 19340074]
56. Zonta F, Mammano F, Torsello M, Fortunati N, Orian L, Polimeno A. Role of gamma carboxylated Glu47 in connexin 26 hemichannel regulation by extracellular Ca: Insight from a local quantum chemistry study. *Biochem. Biophys. Res. Commun.* 2014; 445:10–5. [PubMed: 24468086]
57. Musa H, Fenn E, Crye M, Gemel J, Beyer EC, Veenstra RD. Amino terminal glutamate residues confer spermine sensitivity and affect voltage gating and channel conductance of rat connexin40 gap junctions. *J. Physiol.* 2004; 557:863–878. [PubMed: 15107469]
58. Bukauskas FF, Bukauskiene A, Bennett MVL, Verselis VK. Gating properties of gap junction channels assembled from connexin43 and connexin43 fused with green fluorescent protein. *Biophys. J.* 2001; 81:137–152. [PubMed: 11423402]
59. White TW, Bruzzone R, Wolfram S, Paul DL, Goodenough DA. Selective interactions among the multiple connexin proteins expressed in the vertebrate lens: the second extracellular domain is a determinant of compatibility between connexins. *J. Cell Biol.* 1994; 125:879–892. [PubMed: 8188753]
60. Nakagawa S, et al. Asparagine 175 of connexin32 is a critical residue for docking and forming functional heterotypic gap junction channels with connexin26. *J. Biol. Chem.* 2011; 286:19672–19681. [PubMed: 21478159]
61. Ramanan SV, Brink PR, Varadaraj K, Peterson E, Schirmacher K, Banach K. A three-state model for connexin37 gating kinetics. *Biophys. J.* 1999; 76:2520–2529. [PubMed: 10233068]
62. Teubner B, et al. Functional expression of the murine connexin 36 gene coding for a neuron-specific gap junctional protein. *J. Membr. Biol.* 2000; 176:249–262. [PubMed: 10931976]
63. Oh S, Rivkin S, Tang Q, Verselis VK, Bargiello TA. Determinants of gating polarity of a connexin 32 hemichannel. *Biophys. J.* 2004; 87:912–928. [PubMed: 15298899]
64. Chiquito AJ, Amorim CA, Berengue OM, Araujo LS, Bernardo EP, Leite ER. Back-to-back Schottky diodes: the generalization of the diode theory in analysis and extraction of electrical parameters of nanodevices. *J. Phys. Condens. Matter.* 2012; 24:225303. [PubMed: 22556197]
65. Jaslove SW, Brink PR. The mechanism of rectification at the electrotonic motor giant synapse of the crayfish. *Nature.* 1986; 323:63–65. [PubMed: 3748182]
66. Verselis VK, Ginter CS, Bargiello TA. Opposite voltage gating polarities of two closely related connexins. *Nature.* 1994; 368:348–351. [PubMed: 8127371]
67. Oh S, Rubin JB, Bennett MV, Verselis VK, Bargiello TA. Molecular determinants of electrical rectification of single channel conductance in gap junctions formed by connexins 26 and 32. *J. Gen. Physiol.* 1999; 114:339–364. [PubMed: 10469726]
68. Gutierrez GJ, Marder E. Rectifying electrical synapses can affect the influence of synaptic modulation on output pattern robustness. *J. Neurosci.* 2013; 33:13238–13248. [PubMed: 23926276]
69. Eswar N, Eramian D, Webb B, Shen MY, Sali A. Protein structure modeling with MODELLER. *Methods. Mol. Biol.* 2008; 426:145–159. [PubMed: 18542861]
70. Rocchia W, Sridharan S, Nicholls A, Alexov E, Chiabrera A, Honig B. Rapid grid-based construction of the molecular surface and the use of induced surface charge to calculate reaction field energies: applications to the molecular systems and geometric objects. *J. Comput. Chem.* 2002; 23:128–137. [PubMed: 11913378]

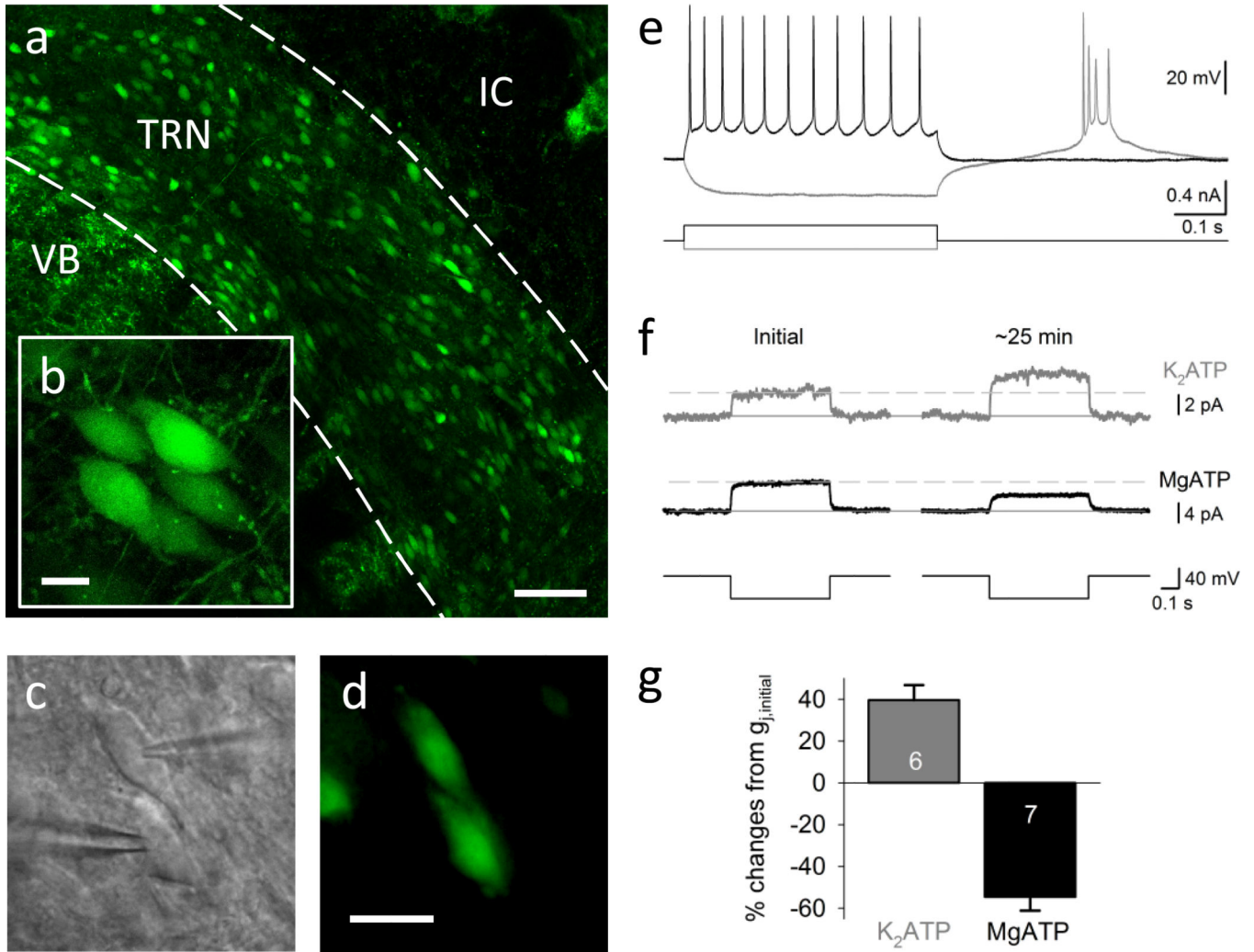


Figure 1. Magnesium dependent plasticity of electrical synaptic transmission between TRN neurons
(a,b) Confocal fluorescence images of horizontal brain slices from a Gjd2-EGFP transgenic mouse showing thalamic reticular nucleus (TRN) interneurons expressing EGFP driven by Cx36 promoter. VB, ventrobasal nucleus of the Thalamus; IC, internal capsule. Scale bars correspond to 100 (a) and 10 (b) μ m. **(c,d)** IR-DIC (c) and fluorescence (d) images of an electrically coupled pair of TRN neurons during dual whole-cell patch clamp. Scale bar correspond to 20 μ m. **(e)** Current-clamp recordings from a TRN neuron showing typical spiking and rebound burst behavior; voltage traces were recorded during 0.5 s current steps of -100 (grey) or 200 (black) pA. **(f)** Voltage-clamp recordings showing averaged transjunctional current traces (10–15 averaged traces) obtained soon after patch openings (initial; left) and after ~25 min of recording (right) for low Mg^{2+} (K_2ATP , top) and high Mg^{2+} ($MgATP$, bottom) conditions; current traces were recorded during 0.5 s transjunctional voltage steps of -40 mV. **(g)** Mean percentage changes of junctional conductance (g_j) from initial values after ~25 min from patch openings with pipette solutions containing 7 mM of K_2ATP (grey) or $MgATP$ (black). Numbers of cell pairs are indicated within columns, and error bars correspond to s.e.m.

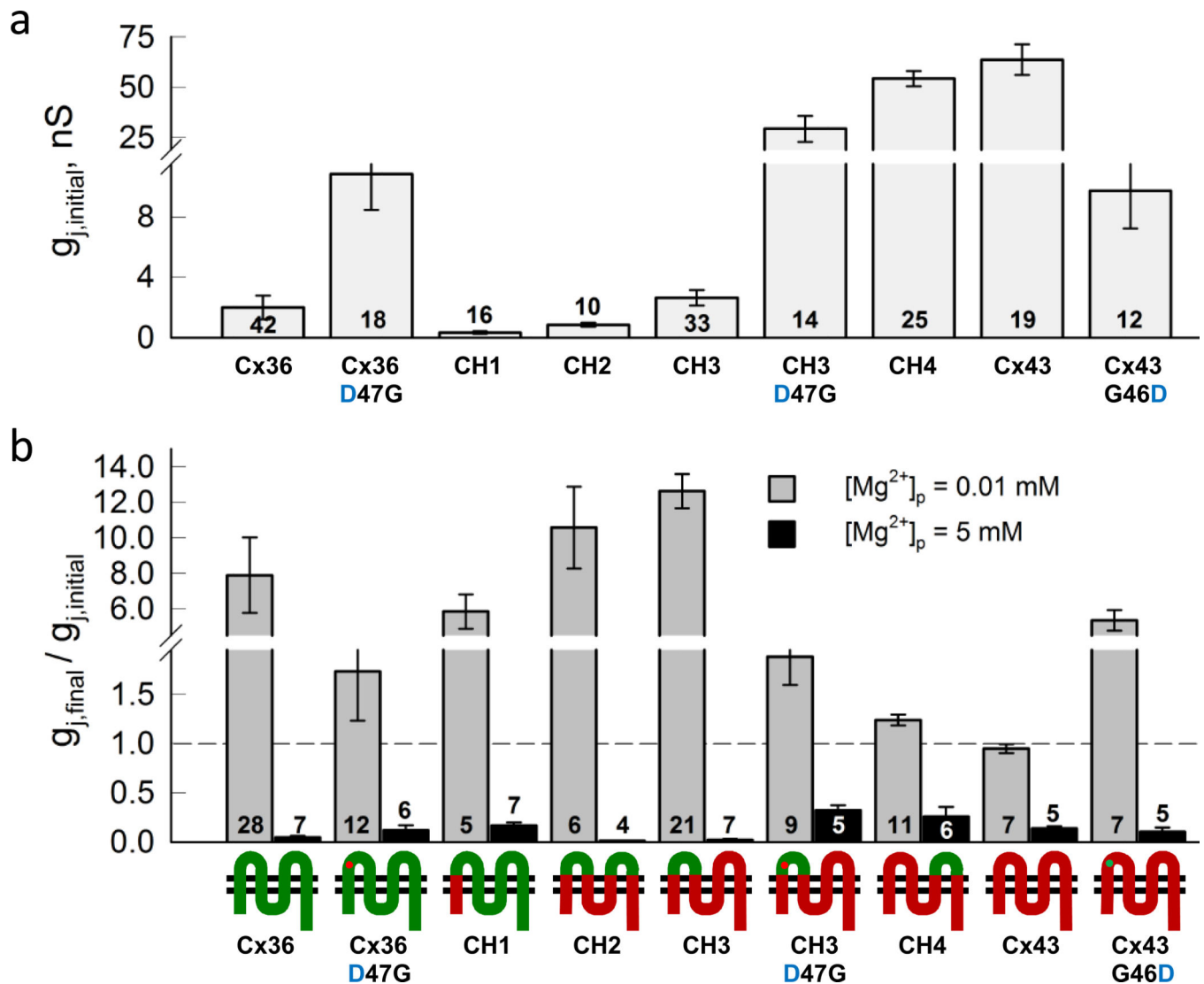


Figure 3. Differences in sensitivity to $[Mg^{2+}]_i$ between Cx36/Cx43 chimeras and mutants
 Experiments were performed in pairs of RIN cells expressing Cx36 (green), Cx43 (red), Cx36/Cx43 chimeras (CH1-CH4), and amino acid substitutions (D47G or G46D). (a) Mean transjunctional conductance measured soon after patch opening ($g_{j,initial}$). (b) Mean g_j (normalized to initial g_j value) measured after ~25 min using pipette solutions containing 0.01 mM (grey) or 5 mM (black) free Mg^{2+} ($[Mg^{2+}]_p$). The dotted line marks the value of normalized g_j equal to 1. Total numbers of cell pairs are indicated within columns, and error bars correspond to s.e.m.

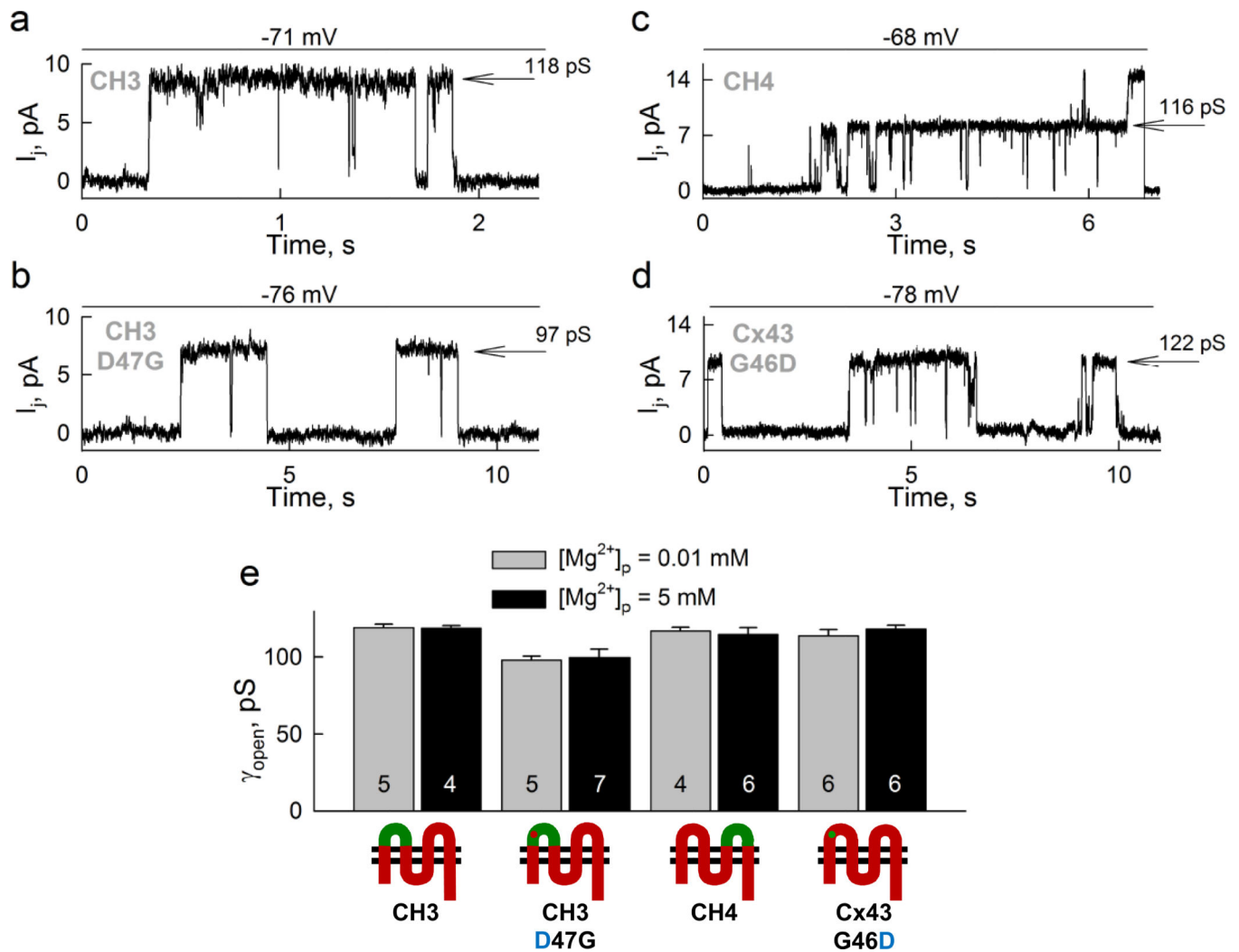


Figure 4. Effect of $[Mg^{2+}]_i$ on single channel conductance from homotypic GJs formed by CH3, CH3*D47G, CH4, or Cx43*G46D
 (a–d) Transjunctional current (I_j) recordings of single channel events obtained at indicated V_j s (top) and using $[Mg^{2+}]_p = 0.01\text{ mM}$. Numbers attached to arrows show single channel conductances at the open state (γ_{open}). (e) Averaged γ_{open} for homotypic GJs formed by CH3, CH3*D47G, CH4, and Cx43*G46D using $[Mg^{2+}]_p = 0.01$ (gray) or 5 (black) mM. Total numbers of cell pairs are indicated within columns, and error bars correspond to s.e.m.

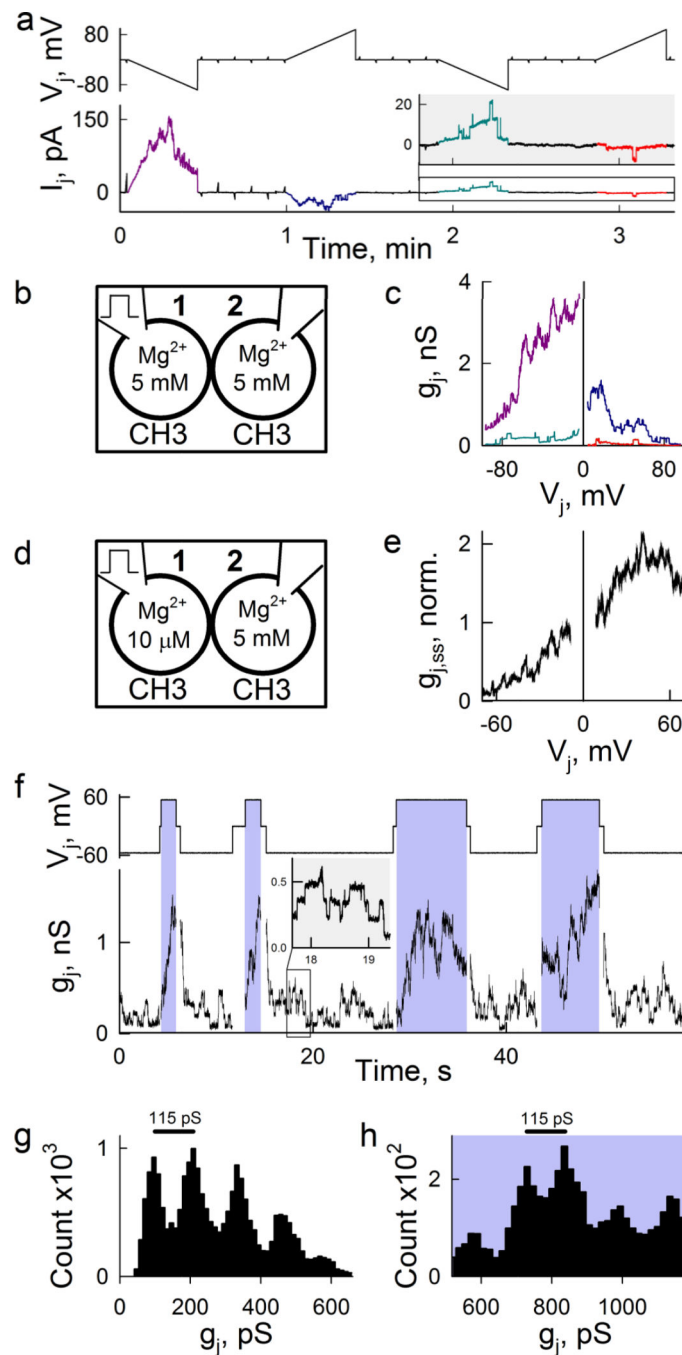


Figure 5. Mg^{2+} Effect on V_j -gating and single channel conductance of homotypic GJs formed of CH3

(a) Changes of I_j (bottom trace) of CH3 GJs in response to repeated 30 s long V_j ramps from 0 to -90 mV and from 0 to $+90$ mV with intermediate small amplitude ramps (-10 mV) (top trace) using symmetric $[Mg^{2+}]_p = 5$ mM. (b,d) Diagrams illustrating $[Mg^{2+}]_p$ in cell-1 and cell-2 and the stimulation site of the V_j protocol for experiments shown in a and c (b), or e (d). (c) g_j - V_j relations obtained from experiment shown in (a). Colors match the I_j data shown in (a). (e) Asymmetric $g_{j,ss}$ - V_j dependence (normalized to g_j value at V_j zero) was

measured by applying V_j ramps from 0 to -70 and from 0 to $+70$ mV (30 s in duration) under transjunctional Mg^{2+} asymmetry shown in **(d)**. Negative potentials applied on the side with low $[Mg^{2+}]_i$ decreased g_j presumably by increasing Mg^{2+} occupancy of the pore through ionophoresis ($n=4$). **(f)** g_j trace (bottom) showing unitary gating events of the homotypic CH3 GJ channel obtained during V_j steps of ± 55 mV (top trace) applied in cell-1 (as illustrated in **(d)**). Negative V_j s facilitated closing transitions, whereas positive V_j s facilitated opening transitions. **(g-h)** Count histograms for all g_j data obtained at negative **(g)** or positive **(h)** V_j s shown in **(f)**. Both histograms show peaks corresponding to the single channel conductance of ~ 115 pS.

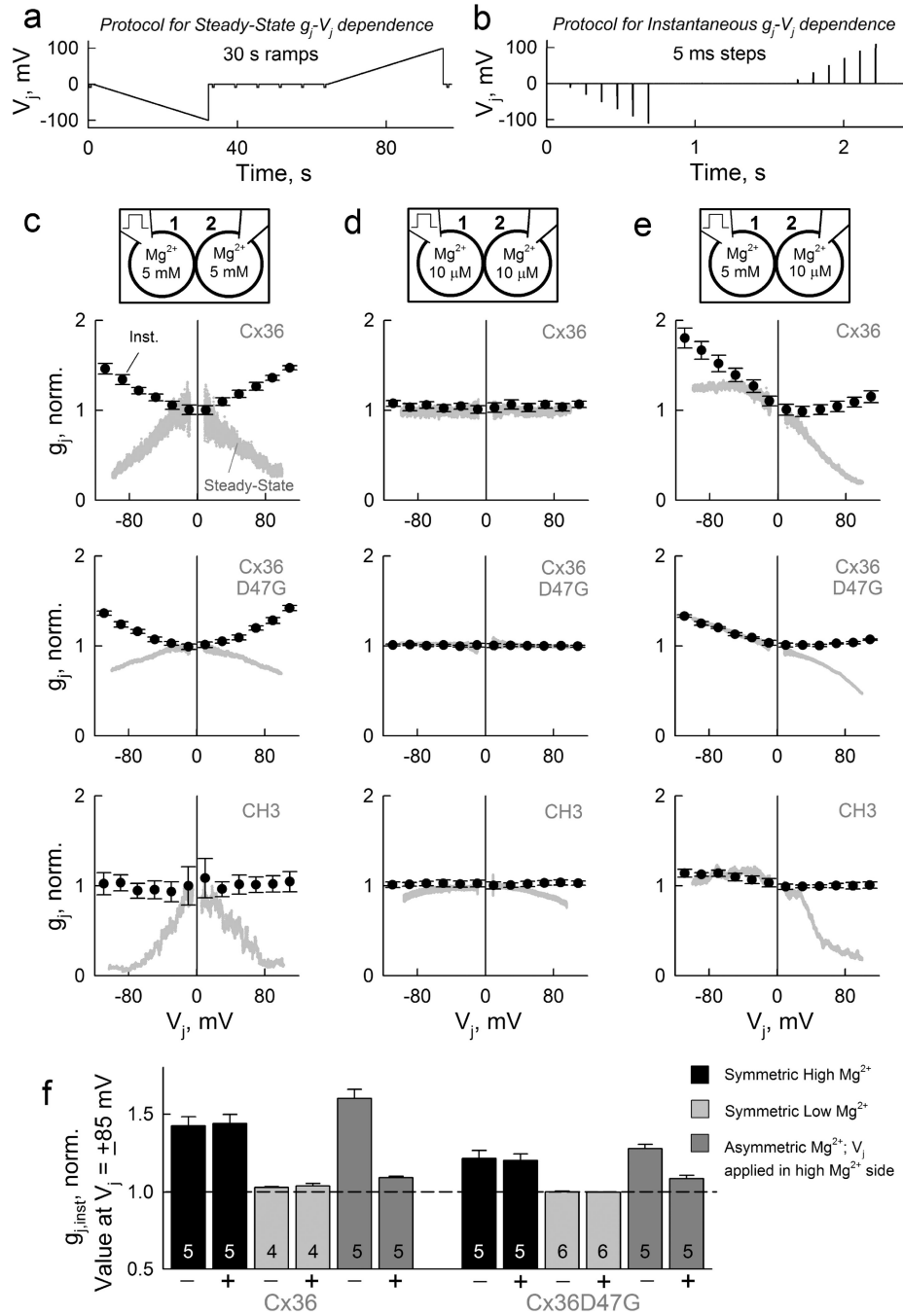


Figure 6. GJs formed by Cx36 show Mg^{2+} -dependent rectification of both steady-state and instantaneous conductance-voltage relationships
(a–b) V_j protocols used to obtain steady-state **(a)** and instantaneous **(b)** g_j-V_j relationships.
(c–e) Steady-state (grey) and instantaneous (black) g_j-V_j relationships (normalized to g_j value at V_j zero) were measured ~30 min after opening of patches under symmetric high **(c)**, low **(d)**, and asymmetric Mg^{2+} conditions **(e)** in homotypic GJs formed of Cx36 (top row), Cx36*D47G (middle row) and CH3 (bottom row). Each data point for instantaneous g_j-V_j relationships was obtained by averaging data from ~10 consecutive V_j protocols shown in

(b), and error bars correspond to s.e.m. Top diagrams in each column show $[Mg^{2+}]_p$ and stimulation site. (f) Mean $g_{j,inst}$ values measured at V_j s equal to -85 and $+85$ mV (normalized to $g_{j,inst}$ value at V_j zero) at symmetric high (black) and low (light gray) $[Mg^{2+}]_p$, and asymmetric Mg^{2+} conditions (dark gray) for GJs formed of Cx36 (left) and Cx36*D47G (right). Total numbers of cell pairs are indicated within columns, and error bars correspond to s.e.m.

Author Manuscript

Author Manuscript

Author Manuscript

Author Manuscript

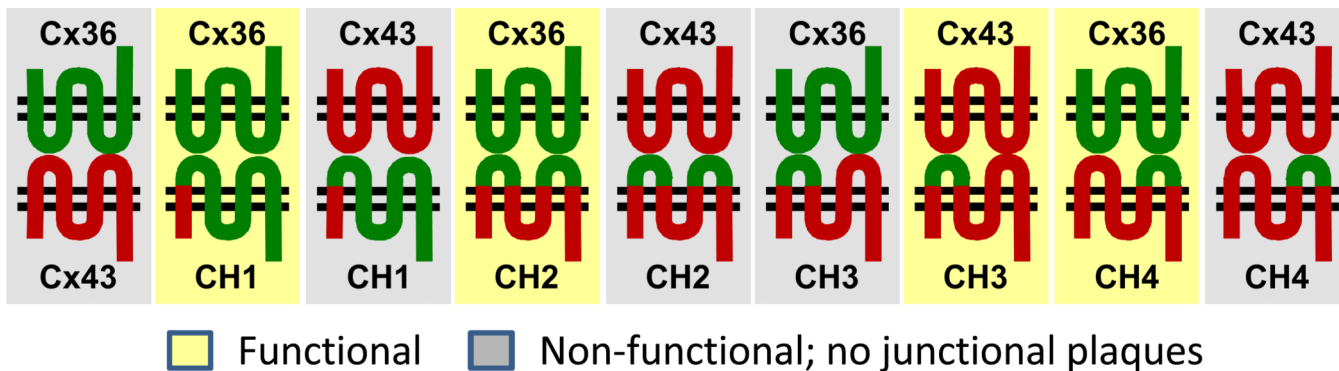


Figure 7. Compatibility between Cx36 and Cx43 GJ channels with functional chimeras
 Among all examined heterotypic combinations between wild type Cx36 (green) or Cx43 (red) with CH1, CH2, CH3, or CH4, only those shown in yellow background formed junctional plaques and exhibit electrical cell-cell coupling, while those shown in grey background did not form junctional plaques or exhibit electrical cell-cell coupling.

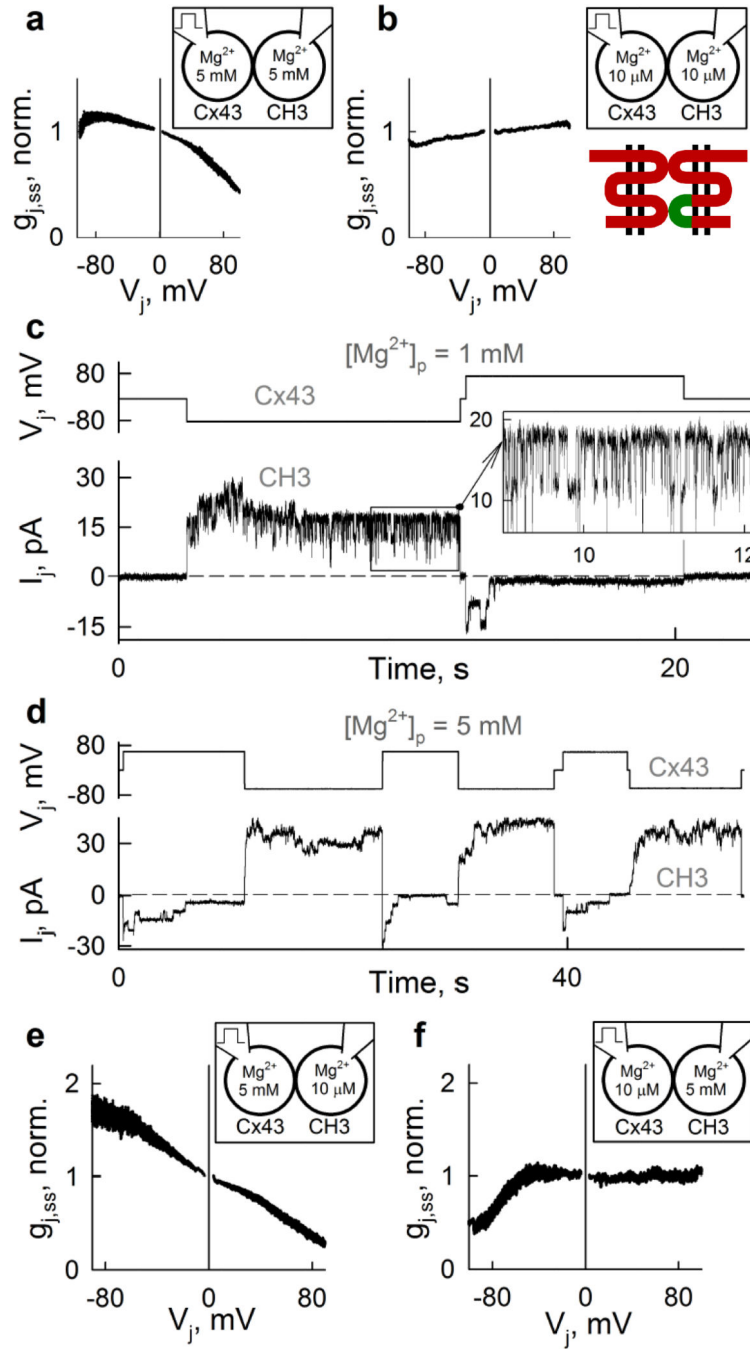


Figure 8. Mg^{2+} -dependent asymmetry in steady-state g_j - V_j relationship and single channel conductance in Cx43/CH3 heterotypic GJs
(a–b) Asymmetric $g_{j,ss}$ - V_j relationships (normalized to $g_{j,ss}$ value at $V_j = 0$, and obtained using the same V_j protocol shown in Fig. 6a) with pipette solutions containing symmetric high (a) or low (b) $[Mg^{2+}]_p$ in heterotypic Cx43/CH3 GJs ($n=5$). Top diagram in each plot shows $[Mg^{2+}]_p$ used in cell-1 and cell-2, stimulation sites and expressed Cxs. **(c)** I_j records of single channel events at symmetric $[Mg^{2+}]_p$ obtained during V_j steps of ± 85 mV (top trace) applied in cell-1 expressing Cx43. **(d)** I_j records (bottom trace) under symmetric high

$[Mg^{2+}]_p$ showing unitary gating events of Cx43/CH3 GJ channel obtained during V_j steps of ± 60 mV (top trace) applied in cell-1 expressing Cx43. Positive V_j s facilitated closing transitions, while negative V_j s facilitated opening transitions. **(e,f)** Asymmetric $g_{j,ss}-V_j$ relationships (normalized to $g_{j,ss}$ value at $V_j=0$) obtained under asymmetric Mg^{2+} conditions (see diagrams) in heterotypic Cx43/CH3 GJs ($n=5$).

Author Manuscript

Author Manuscript

Author Manuscript

Author Manuscript

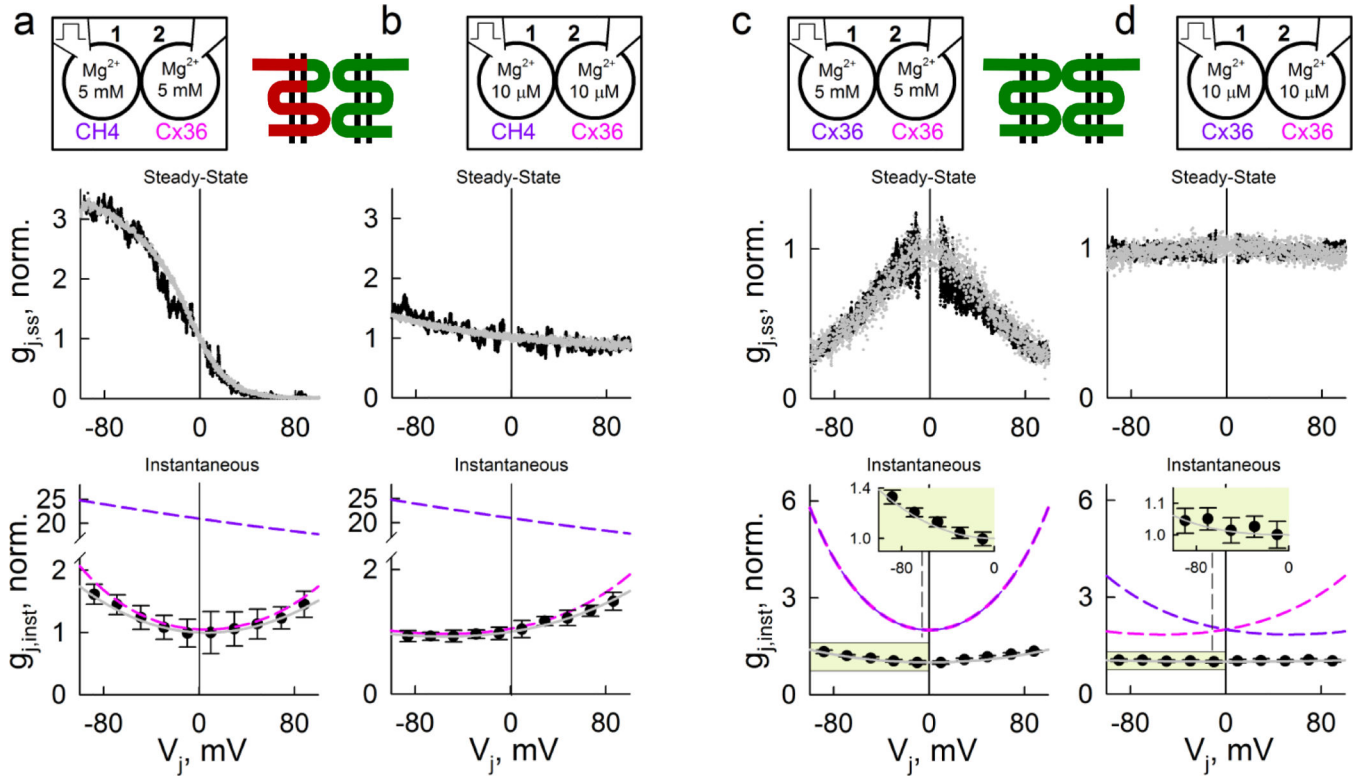


Figure 9. Mg^{2+} -dependent asymmetry in steady-state and instantaneous g_j-V_j relationship in Cx36/CH4 heterotypic GJs

(a–b) Asymmetric steady-state (top) and instantaneous (bottom) g_j-V_j relationships shown in black (normalized to g_j value at $V_j=0$, and obtained using the same V_j protocol shown in Figs. 6a and 6b, respectively) obtained under symmetric high (a) and low (b) $[Mg^{2+}]_p$ in heterotypic Cx36/CH4 GJs ($n=5$). The top diagram in each plot shows $[Mg^{2+}]_p$ used in cell-1 and cell-2, stimulation sites and expressed Cxs. Each data point for $g_{j,inst}-V_j$ relationships was obtained by averaging data from ~10 consecutive V_j protocols, and error bars correspond to s.e.m. Simulated curves shown in grey for steady-state (top) and instantaneous (bottom) g_j-V_j relationships were obtained using the S4SM. Dotted lines show $g_{j,inst}-V_j$ relationships for CH4 (purple) and Cx36 (pink) aHCs used in simulation of steady-state and instantaneous g_j-V_j relationships. (c–d) Symmetric steady-state (top) and instantaneous (bottom) g_j-V_j relationships for homotypic Cx36 GJs are shown in black (data from Fig. 6c,d). Simulated curves shown in grey were obtained using the S4SM and similar rectification parameters were obtained from Cx36 aHCs shown in (a) and (b). All parameters for simulation are reported in Supplementary Table 1.

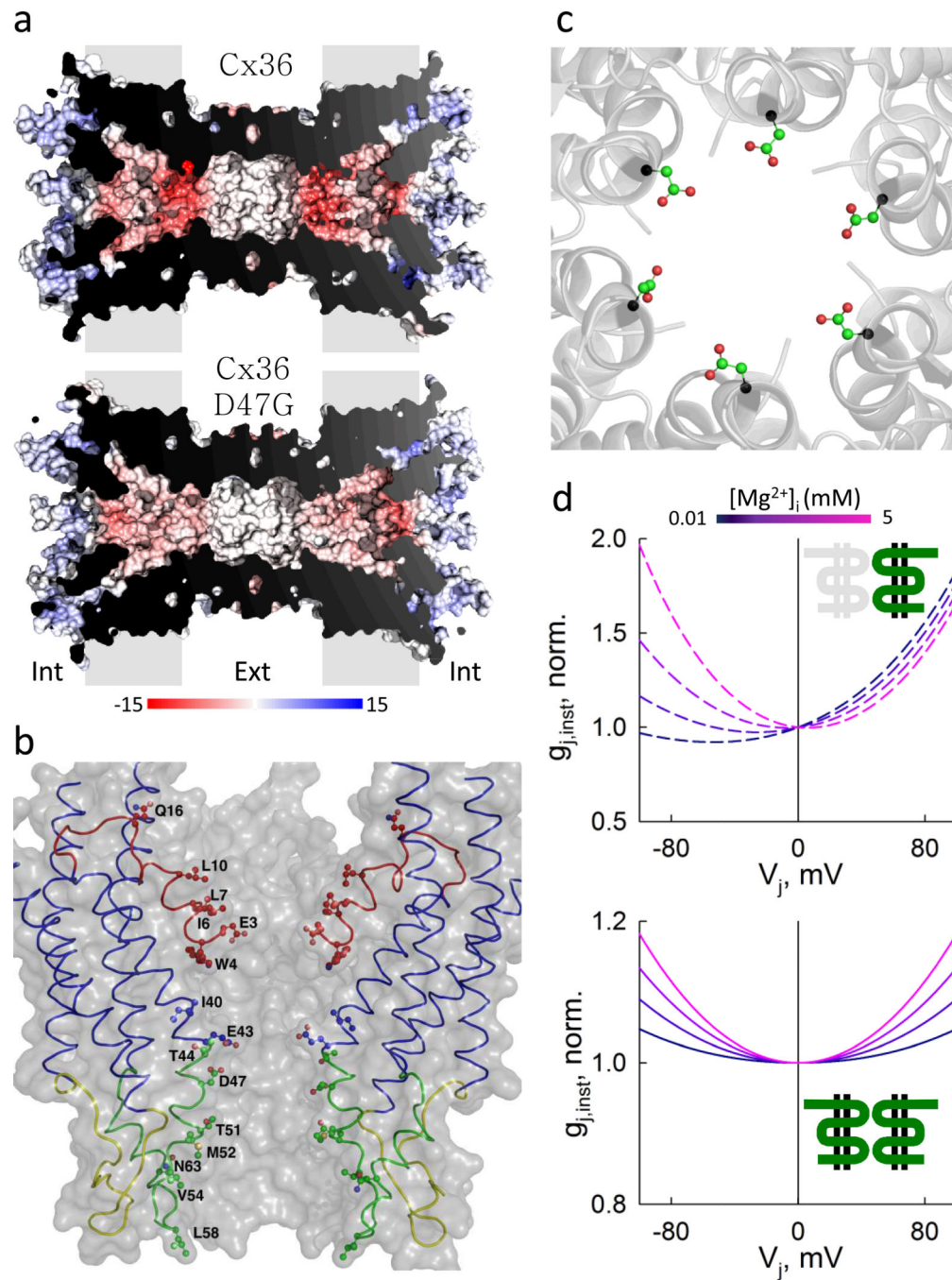


Figure 10. Homology models of Cx36 and Cx36*D47G GJ channel structure and Mg²⁺-dependent modulation of instantaneous rectification

(a) Cross-sections of GJ channels formed by Cx36 (top) or Cx36*D47G (bottom) generated by sequence homology to Cx26 crystal structure. Electrostatic surface potential is displayed for both channels and was estimated with DELPHI (see Methods). The color bar at the bottom represents electrostatic surface potentials ranging from -15 (red) to 15 (blue) $kT e^{-1}$. (b) Side view of a Cx36 aHC indicating the pore-lining residues of only two Cx subunits represented with thin ribbon style (principal chain). Main domains of Cx subunits are

depicted with different colors and the side chains of pore-lining residues are represented with sticks and spheres. (c) View of the pore from the center of the channel towards the cytoplasmic mouth. The six D47 residues are displayed with sticks and spheres to illustrate the orientation and position of their side chains with respect to the lumen of the channel. (d) Normalized $g_{j,\text{inst}}-V_j$ plots for aHCs (top) and GJ channels (bottom) formed by Cx36 generated using different values for Mg^{2+} -dependent coefficient (r_{Mg}) with the S4SM of GJ channels gating. Color bar at the top represents different $[\text{Mg}^{2+}]_i$ from 0.01 to 5 mM.

Author Manuscript

Author Manuscript

Author Manuscript

Author Manuscript